Stratiform cloud electrification: comparison of theory with multiple in-cloud measurements

Article

Accepted Version

Stratiform cloud electrification: comparison of theory with multiple in-cloud measurements

K.A. Nicoll and R.G. Harrison

Department of Meteorology, University of Reading, Reading, Berkshire, UK, RG6 6BB

Abstract

Stratiform clouds constitute ~40% of global cloud cover and play a key role in determining the planetary radiation budget. Electrification remains one of the least understood effects on their microphysical processes. Droplet charging at the top and bottom edges of stratiform clouds arises from vertical current flow through clouds driven by the Global atmospheric Electric Circuit. In-cloud charge data are central in assessing the role of charge in droplet growth processes, which influence droplet size distributions and associated cloud radiative properties and precipitation. This study presents the first high vertical resolution electrical measurements made in multiple layer clouds. Of the 22 clouds sampled, all were charged at their edges, demonstrating unequivocally that all stratiform clouds can be expected to contain charge at their upper and lower boundaries to varying extent. Cloud base and cloud top are shown to charge asymmetrically, with mean cloud top space charge +32 pCm^{-3} and base space charge -24 pCm^{-3}. The larger cloud top charges are associated with strong temperature inversions and large vertical electrical conductivity gradients at the upper cloud boundary. Greater charging was observed in low altitude (<2km) clouds (20.2 pCm^{-3}), compared to higher altitude (>2km) cloud layers (7.0 pCm^{-3}), consistent with the smaller air conductivity at lower altitudes caused by reduced cosmic ray ionisation. Taken together, these measurements show that the greatest cloud droplet charges in extensive stratiform clouds occur at cloud tops for low altitude (<2km) clouds, when vertical mixing is suppressed by appreciable temperature inversions, confirming theoretical expectations. The influence of cloud dynamics on layer cloud edge charging reported here should inform modelling studies of cloud droplet charging effects on cloud microphysics.

1. Introduction

Earth's atmosphere is a weak conductor of electricity due to the presence of atmospheric cluster ions, formed, near the surface, from natural radioactivity in rock and soil, and at higher altitudes by Galactic Cosmic Rays (GCRs). GCRs are the primary source of ionisation above the Earth's surface, creating a cascade of charged energetic particles by collision with O_2 and N_2 molecules as they enter the atmosphere from above. The presence of cluster ions, and the existence of a Global atmospheric Electric Circuit (GEC) permit a small current density, J_c, ($\sim 10^{-12}$ A m^{-2}) to flow vertically from the lower ionosphere (approx. 60km altitude) to Earth's surface (e.g. Wilson, 1929; Israel, 1971). This provides a link between the upper atmosphere and the lower troposphere, in all fair weather regions of the globe. Conventional atmospheric electricity (e.g. Israel, 1971) distinguishes between disturbed weather (i.e. thunderstorm conditions) and fair weather regions (where there is no local charge generation), but there also exists a very common, but seldom mentioned, situation of semi-fair weather conditions – defined here as conditions pertaining to extensive, non-precipitating layer clouds. These are different from electrified shower clouds which, like thunderstorms, contribute significantly to the GEC current flow (e.g. Mach et al, 2011; Blakeslee et al, 2014) and are typically associated with precipitation. Layer clouds are prevalent, covering almost 40% of the planet's surface at any one time (Klein and Hartmann 1993), and play a large role in the terrestrial radiation balance. When such extensive clouds are present, the fair weather current must pass through the cloud (experimentally verified by Bennett and Harrison, 2009 and Nicoll and Harrison, 2009; modelled by Baumgaertner et al, 2014). The consequence of current flow through cloud layers is for charge accumulation to occur at the top and bottom horizontal cloud edges (Tinsley 2000, Zhou and Tinsley 2007), due to the conductivity transition between the clear air and cloudy regions (see e.g. Harrison et al 2015, figure 1). We define the horizontal cloud edge here as the transition that occurs between cloud and cloud-free air at the cloud base or top (not the sides of the cloud).

Charging of cloud droplets has implications for their behaviour and can affect cloud microphysical processes such as droplet-droplet interactions (e.g. Khain et al, 2004), aerosol-droplet interactions (e.g.

Tinsley et al, 2000) and droplet activation (e.g. Harrison and Ambaum, 2008). Harrison et al 2015 discuss these mechanisms in detail. The magnitude of cloud droplet charge required to affect each of these cloud microphysical processes varies between a few electronic charges to a few thousand, depending on the process and the droplet size. The likely large scale effect of charge on the cloud droplet population is a change in size or number concentration of the droplets, which can lead to a change in the radiative properties of the cloud, and potentially precipitation changes. This is supported by recent observations of changes in cloud base properties associated with well-known atmospheric electrical variations (Harrison and Ambaum, 2013; Harrison et al 2013). As stratus clouds are common globally (being particularly prevalent over oceanic regions), (Klein and Hartmann, 1993) and the vertical current is always present in semi-fair weather regions, electrical microphysical effects may provide an underlying source of variability in cloud properties.

Characterisation of the typical droplet charge in layer clouds is a key factor in understanding cloud edge electrical effects, and is at present not well known. Previous measurements of cloud droplet charging in non-thunderstorm cloud have mostly been made from mountaintop observatories in the 1950s (e.g. Twomey, 1956 Phillips and Kinzer, 1957; Allee and Phillips, 1959), where droplet charges of typically ±20 elementary charges (*e*) were found (Phillips and Kinzer, 1958). There remain, however, concerns that the electrical conditions at mountaintops are not representative of meteorological conditions in clouds in the free atmosphere. Aircraft measurements of droplet charging were made by Beard et al (2004) within altostratus, although charge measurements were only reported for the middle of the cloud rather than on the upper and lower edges, where the charge accumulates. In the UK, balloon borne measurements by Jones (1957) and Jones et al (1959) demonstrated appreciable gradients in electric field and conductivity at horizontal cloud edges inside a stratiform cloud layer, whilst half a century later Nicoll and Harrison (2010) reported high vertical resolution charge measurements from a similar free balloon platform through a layer of stratocumulus cloud. A region of negative charge (up to -35pC m^{-3}) was found at cloud base, with a magnitude similar to that predicted by theory. These sparse measurements confirmed the existence of charging at upper and lower edges of layer clouds, however further

quantitative study of the location, polarity and magnitude of charge carried by cloud droplets in layer clouds is required to inform modelling studies of charge influences on cloud microphysical processes.

This paper presents a unique new dataset of observations of layer cloud charging at horizontal edges using specially designed charge and cloud instrumentation flown from free balloon platforms. Quantitative analysis of the electrical characteristics of a large number of stratiform cloud layers is reported, providing a new dataset with which to better understand the role of electrification in layer clouds. In section 2 the theory behind accumulation of charge on cloud edges is discussed, whilst in section 3 the instrumentation is described. Section 4 presents new measurements of edge charging for multiple clouds, and section 5 discusses the various factors controlling cloud edge charging in terms of the measurements obtained. Section 6 discusses estimates of individual cloud droplet charges, whilst section 7 includes a discussion and section 8 presents the conclusions.

2. Separation of charge at edges of extensive layer clouds

Charge accumulation is associated with the upper and lower horizontal edges of layer cloud due to the transition in electrical conductivity, σ_t, between clear air and droplet laden air. Droplet laden air has a lower conductivity (i.e. higher resistivity) than clear air due to the attachment of cluster ions (typically nm diameter) to the cloud droplets (typically μm diameter). The horizontal cloud edge boundary region therefore has an associated vertical gradient in conductivity, with, in turn, a vertical gradient in the electric field, E. From Gauss' law of electrostatics, the change in the vertical component of the electric field E_z gives rise to a region of space charge of density, ρ, (defined as the net difference between positive and negative charge per unit volume):

$$\frac{dE_z}{dz} = -\frac{\rho}{\varepsilon_0} \qquad 1,$$

where ε_0 is the permittivity of free space and z is positive upwards. Assuming Ohm's law in the vertical direction, and expressing E_z in terms of conductivity σ_t, (where the subscript t denotes the total

conductivity, i.e. the contribution from both positive and negative conductivities) and the atmospheric potential gradient, PG, where PG = $-E_z$ and

$$J_c = \sigma_t PG \quad (2)$$

it follows that equation 1 can be re-written to give ρ in terms of the fair weather conduction current density, J_c, as

$$\rho = -\varepsilon_0 J_c \frac{d}{dz}\left(\frac{1}{\sigma_t}\right) = -\varepsilon_0 J_c \frac{1}{\sigma_t{}^2}\left(\frac{d\sigma_t}{dz}\right) \quad (3)$$

The electrical changes which occur across a layer cloud are illustrated conceptually in Figure 1, for an assumed conductivity gradient at the upper and lower horizontal cloud boundaries. If the gradient is made sharper, a larger amount of space charge but over a narrower layer results. As will become apparent, this example is very much that of an idealised cloud layer.

The polarity of the charge layers generated by the vertical conductivity change is, accordingly, positive at the top and negative at the base of the cloud, due to the difference in the direction of the vertical conductivity gradients between the upper and lower cloud edges and the downward direction of the current flow. From the instant that cloud droplets start to form, a vertical gradient in conductivity will become established and charge will accumulate in these regions. The horizontal charge layers created at upper and lower horizontal cloud boundaries are maintained by the current flow through the cloud, which ensures a continuous supply of ions into the top and bottom of the cloud.

It is clear from equation 3 that cloud edge charging depends on the vertical conductivity gradient which will be determined by local meteorological conditions, as well as the fair weather current density, J_c. It follows that modulation of J_c, either from external sources such as GCR flux changes due to the solar magnetic field, or internal sources such as a change in thunderstorm generators in the GEC, will also modulate the space charge (e.g. Nicoll, 2014, Mach et al, 2011). This is discussed in more detail in section 7. A further consideration, as pointed out by Harrison et al (2015) is the variations with height which

occur in the cosmic ray ion production rate and therefore in σ_t. The associated expectation is that the cloud edge charging will vary with the height dependence in σ_t, assuming similar vertical profiles in the cloud droplet properties at different heights.

3. Methodology

3.1 Cloud and charge instrumentation

To estimate the typical charges on cloud droplets, knowledge of both the in situ cloud properties and charge profiles are required. A meteorological radiosonde provides a suitable platform with a typical vertical sampling resolution of ~5m from its ascent rate of ~5ms^{-1} and sampling rate of 1Hz. The standard radiosonde only measures pressure, temperature, relative humidity (PTU) and position, however a specially developed data acquisition system known as PANDORA (Programmable ANd Digital Operational Radiosonde Accessory) (Harrison et al, 2012), allows the attachment of additional science sensors, and transmission of the data synchronously with the PTU data. Adopting this approach, an optical cloud droplet sensor has been developed to provide information on the cloud droplet profile and determine the thickness of the cloud to clear air transition (which is generally not well studied, either at horizontal cloud edges or vertical ones, as the so called "twilight zone" demonstrates (Koren et al, 2007)). The sensor employs a backscatter method using an ultra-bright Light Emitting Diode (LED) at 590nm as the source, with a photodiode receiver (Harrison and Nicoll, 2014). The cloud droplet sensor returns a measurement of visible range, X_r, which shows considerable change at the cloud edge boundary (which occurs in the same region as the conductivity changes). The photodiode also provides a direct measurement of solar radiation, which provides a further independent determination of the cloud edge boundary region in daylight (Nicoll and Harrison, 2012). In addition, a small charge sensor is flown alongside the optical cloud droplet sensor to measure the net space charge density within the cloud layer. This employs a spherical electrode connected to a sensitive electrometer. It primarily responds to induced displacement currents generated by electric field changes as the sensor moves through the cloud layer (Nicoll, 2013). Details of the space charge derivation from the measurement of charge sensor current are given in the appendix.

157 The combined package of the PANDORA, optical cloud droplet sensor and charge sensor has a mass of
158 250g and is attached to the side of a standard Vaisala RS92 radiosonde, all flown under a 200g helium
159 filled carrier balloon.
160
161 A useful comparison can be made between the space charge profile measured by the charge sensor and
162 that calculated from theory. This can be achieved from the data measured by the cloud droplet sensor,
163 which can be used to estimate the vertical in cloud conductivity profile, and equation 3. To estimate the
164 conductivity profile one must first consider the droplet concentration profile through the cloud layer. The
165 cloud droplet sensor was laboratory calibrated to provide optical extinction, ξ, by measuring the
166 transmission of LED light through a region of droplet laden air simultaneous with the optical backscatter
167 (Harrison and Nicoll, 2014). The optical extinction is related to the visual range, X_r, by

168 $$X_r = \frac{\ln \varepsilon}{\xi} \qquad 4,$$

169 where ε is normally taken to be 0.05 (HMSO, 1982) (see e.g. Harrison, 2012). Assuming an optical
170 extinction coefficient for cloud droplets of approximately twice their projected area (e.g. Bohren and
171 Huffman 1983; Harrison 2012), the total extinction coefficient ξ is related to the droplet diameter, d, and
172 droplet number concentration, Z_d by

173 $$Z_d = \frac{2\xi}{\pi d^2} \qquad 5.$$

174 Thus, by assuming an average cloud droplet diameter (taken here to be 10μm – a typical cloud droplet
175 size for stratocumulus cloud (Miles et al 2000)), Z_d can be estimated. The cloud droplet number
176 concentration is a key parameter in calculating the conductivity profile through the cloud layer. Using the
177 steady state ion-balance equation (see e.g Harrison and Carslaw 2003), which characterises the ion
178 concentration in the presence of cloud droplets, the total conductivity is

179 $$\sigma_t = \frac{\mu e}{\alpha}\left(\sqrt{(\beta_a{}^2 Z_a{}^2 + 2\beta_a Z_a \beta_d Z_d + \beta_d{}^2 Z_d{}^2 + 4\alpha q_i)} - (\beta_a Z_a + \beta_d Z_d)\right) \qquad 6,$$

where μ is the mean ion mobility (taken here as 1.7×10^{-4} m^{-2} V^{-1} s^{-1}), e, the elementary charge (1.6×10^{-19} C), α the ion-ion recombination coefficient (1.6×10^{-12} m^{-3} s^{-1}), Z_a the background aerosol number concentration (assumed here to be 1000 cm^{-3}), and β_a and β_d the size-dependent ion-aerosol and ion-droplet attachment coefficients respectively (Gunn, 1954). Equation 6 assumes that the bipolar ion concentrations are equal and represents the cloud droplets by a single (monodisperse) size. q_i is the ion production rate per unit volume (typically 2 ion pairs cm^{-3} s^{-1} near the surface) which is described in more detail in the following paragraph. There is likely to be considerable variability in many of the parameters in equation 6 in real cloud environments, particularly in terms of Z_a and the mean aerosol radius, on which β_a depends, therefore a considerable range of values for σ_t is expected. Application of equations 4 to 6 to the cloud droplet sensor data allows the estimation of σ_t from the optical sensor, which can be applied to equation 3 to derive an estimate of the in-cloud space charge.

3.2 Ionisation instrumentation

Equation 6 demonstrates that knowledge of the ion production rate, q_i is required to derive the conductivity. Using additional instrumentation to detect the vertical profile of ionisation, q_i was measured directly on some of the charged cloud flights. This approach uses two Geiger tubes (LND714) with a compact high tension voltage supply, and an interval timing technique for improved resolution at low count rates (described by Harrison et al 2013). The electrical conductivity of air depends directly on the ion production rate, which varies as a function of altitude and latitude, and plays a role in determining the cloud edge charge through equation 3. Over land, near the surface, ions are generated from natural radioactivity such as radon gas (4 to 8 ion pairs cm^{-3} s^{-1} (Hirsikko et al 2007)), which are typically lofted to altitudes of 1-2 km within the atmospheric boundary layer. Galactic Cosmic Rays (GCRs) provide an additional source of ionisation of around 2 ion pairs cm^{-3} s^{-1} at the surface, which increases approximately exponentially with altitude to become the dominant ion source, reaching a maximum (the Regener-Pfotzer maximum) at ~20 km (e.g. Bazilevskaya et al, 2008). A consequence of the increase in ion production rate means that the conductivity also increases with height from a few fS m^{-1} at the surface to

206 a few pS m^{-1} at 20 km. From equation 3, the space charge generated at cloud edges is proportional to
207 $1/\sigma_t^2$, therefore, since σ_t varies with height, ρ is also expected to vary. This prediction is tested in section
208 5 using the measurements of ionisation rate obtained from the balloon Geiger sensor.
209
210 **4. Charged cloud measurements**
211 **4.1 Typical stratiform cloud**
212 To investigate layer cloud charging, a series of specially instrumented balloon flights were carried out
213 during 2013-2015, primarily from the Reading University Atmospheric Observatory (RUAO), UK (51.44° N,
214 0.95° W), but also from Hyytiala, Finland (61.85°N, 24.30°E), and Halley, Antarctica (75.35°S, 26.66°W).
215 Low altitude non frontal stratus and stratocumulus clouds of large horizontal extent (8/8ths cloud cover
216 from a single site) were targeted since cloud edge charging is expected from theory to be at its greatest
217 with sharp cloud boundaries which require little vertical mixing, and at low altitudes (<5km) where σ_t has
218 its smallest values.
219
220 Figure 2 shows data from an instrumented balloon flight through stratocumulus cloud over RUAO on 18th
221 November 2013, which had properties typical of stratiform cloud at Reading. From the thermodynamic
222 measurements measured by the radiosonde (Figure 2(a)), the temperature inversion at 1.2km indicates
223 the cloud top, however, combined with the RH determination, the position of the cloud base is much
224 more ambiguous. In contrast, both the optical cloud droplet (Figure 2(b)) and charge sensor (Figure 2(d))
225 show the cloud boundary regions very distinctly, with the location of the lower and upper cloud edges
226 clearly at 0.85 and 1.2km respectively. Inside the cloud the visual range measured by the optical sensor
227 decreases to 120m (from >1000m outside the cloud), and the solar radiation increases as the sensor
228 travels upwards through the cloud layer, consistent with the decrease in optical depth. Figure 2 (d)
229 demonstrates space charge of up to ± 160pCm^{-3} at both the upper and lower cloud edges, with very little
230 charge in the middle of the cloud. The fact that the charge is concentrated in narrow layers at these cloud
231 edges suggests that the mixing processes removing the charge occur at a lesser rate than the charging

232 rate. In addition, the opposite polarity of charging between the upper and lower cloud boundaries
233 (positive at cloud top, and negative at cloud base), in this case, agrees well with that predicted by the
234 theory outlined in section 2.
235
236 The conductivity profile calculated from the estimation of Z_d and equations 4, 5 and 6 is plotted in Figure
237 2 (c), where it is seen that the presence of the cloud layer decreases the conductivity substantially (from
238 approx. 10 fSm^{-1} to 2 fSm^{-1} from outside the cloud to inside), generating the expected vertical gradient in
239 conductivity on the horizontal cloud edges. Also shown in Figure 2 (c) is the estimated potential gradient
240 profile through the cloud layer, which is calculated from the derived σ_t profile and equation 2, assuming
241 that J_c is constant through the cloud layer (with J_c = 2pA m^{-2}). Note the similarity in the mean structure
242 between the theoretical profiles in Figure 1 and the measured ones in Figure 2. Finally, the predicted
243 cloud edge space charge, shown in Figure 2 (d) in grey, can be calculated from equation 3, again with J_c =
244 2pA m^{-2}, and using σ_t calculated from equation 6. Figure 2 (d) also depicts the space charge measured
245 directly by the cloud sensor (in black), demonstrating good agreement between the locations of the
246 predicted and measured charge layer, as well as the polarity. In this cloud layer, both the predicted and
247 observed charge is located at the cloud edge regions, where there is a vertical gradient in cloud droplet
248 number and size and therefore a conductivity gradient. It should be noted that exact agreement between
249 the measured and theoretical profiles is not expected as the theory is based on a very simple (and static)
250 view of clouds, and does not incorporate any vertical mixing which is known to exist in stratiform clouds
251 (e.g. Shupe et al, 2008). The magnitude of the calculated charge is somewhat smaller than that measured,
252 but this varies with the assumptions made in equations 3-6, unlike the location of the charge layers, which
253 depends solely on the location of the vertical conductivity gradient and therefore the vertical gradient in
254 cloud droplet concentration. This sensitivity can be illustrated by perturbing the assumed values:
255 increasing the value of J_c from 2 to 3 pAm^{-2} and decreasing q_l from 2 to 1 $cm^{-3}s^{-1}$ increases the maximum
256 predicted space charge from 37 to 111 pCm^{-3}.
257

4.2 Horizontal distribution of charge within cloud layer

As the vertical current flows througout all fair weather regions of the atmosphere, cloud edge charging is expected across the entire horizontal extent of an extensive layer cloud. Preliminary experimental evidence for this was given in Rycroft et al (2012) and is further supported here. Figure 3 shows data from an ascent and descent of an instrumented balloon through the same stratiform cloud layer, measured 105km apart. Figure 3(a) shows the GPS derived location of the balloon during its ascent from Reading (black) and descent (grey), and (b) an infrared satellite image showing large scale low cloud coverage of the southern UK at the time of the balloon launch. Figures 3 (c) to (f) show both ascent (black) and descent (grey) data from the instrumented balloon flight, whereby a cloud layer exists between 0.7 and 1 km (the lower part of the descent data is missing due to loss of the radiosonde signal close to the ground). This comparison demonstrates that all four profiles of temperature, RH, visual range and charge are similar between ascent and decent, with a slight lowering of the cloud top on the descent compared with the ascent. The charge sensor's response became saturated at its maximum value on both the ascent and descent stages of the flight at the cloud top (red points), suggesting a very large concentration of positive charge near the upper cloud edge. For this particular flight, saturation of the charge sensor would have occurred at approximately 200pCm^{-3} therefore it is likely that the charge at cloud top exceeded this value. In contrast there is little evidence of a charge layer at the cloud base. The asymmetry in charge between cloud base and top is likely to be related to the large temperature inversion (of 10°C), which leads to a particularly strong gradient in the visual range at cloud top (Figure 3(e)). From equation 3, this sharp thermodynamic transition from cloudy to clear air will result in a strong gradient in conductivity at the cloud top, with the expectation of substantial positive space charge accumulations: this is supported by the charge data shown in Figure 3(f)). The substantial variability in the charge within the main body of the cloud (up to +/- 100 pCm^{-3} which is larger than on most of the flights observed), with a gradual transition from positive to negative charge as cloud base is approached, may provide an explanation for the lack of a well defined charge layer at cloud base, despite a clear gradient in visual range at cloud base. It is possible that downward mixing of the large amount of positive charge at cloud top acts to neutralise some of the negative charge at the cloud base, thus resulting in the observed slightly negative values

285 towards the base of the cloud layer. Regardless of the explanation for the unusual charging behaviour,
286 the existence of substantial charge at a similar height in the cloud but widely horizontally separated
287 therefore confirms that cloud edge charging is a horizontally widespread phenomena.
288
289 **4.3. Multiple cloud layers**
290 An interesting case of cloud edge charging occurs when multiple, vertically-displaced but overlapping
291 cloud layers exist. Figure 4 shows vertical profiles from an instrumented balloon flight through two
292 distinct cloud layers between 0.7-1.0km and 1.4-1.6km (visual range was not available on this flight).
293 Figure 4 (c) demonstrates the presence of bipolar space charge in both layers, each with positive charge
294 at cloud top and negative charge at cloud base, in agreement with the theory set out in section 2. The
295 magnitude of the space charge in the upper cloud layer is much smaller than that in the lower cloud layer,
296 which is likely related to a shallower conductivity gradient between clear and cloudy air in the upper cloud
297 layer. This is likely to result from 1) differences in the cloud droplet profiles between the two clouds, with
298 lower liquid water content expected in the upper cloud layer and 2) an increase in the ion production rate
299 in the upper cloud layer which acts to reduce the conductivity gradient (as modelled by Zhou and Tinsley
300 2007). The effect of variations in ionisation rate on cloud edge charging is discussed more fully in
301 section 5. Nevertheless, the presence of space charge in both cloud layers confirms the continuity of
302 current density through the upper cloud layer to the layer below, allowing the distinct cloud layers directly
303 above each other to both become charged at their horizontal boundaries.
304
305 **4.4 Summary of all stratiform cloud flights**
306 Section 4.1 demonstrates a typical example of a stratiform layer cloud and the parameters measured by
307 the specially-instrumented radiosondes. The current section summarises the 22 different stratiform cloud
308 layers sampled to date in order to quantify the variability between different cloud layers. The properties
309 of the 22 stratiform cloud layers analysed are summarised in Table 1.
310

311 Table 1 demonstrates that the range of cloud base heights sampled was from from 475 to 4838m, with a
312 median height of 1367m , with cloud depths (i.e. cloud top height minus cloud base height) ranging from
313 the shallowest cloud layer of 86m to the deepest of 1700m (median cloud depth 285m). The mean space
314 charge density in each cloud layer varied between 2 to 43 pC m^{-3}, with a median of 16 pC m^{-3}, with the
315 maximum space charge density in each cloud layer ranging from 10 to 253 pC m^{-3} (median = 109 pC m^{-3}).
316 These values are calculated from the magnitude of the charge only, as taking the polarity into account
317 results in values very close to zero due to the presence of opposite polarity charge at cloud base and cloud
318 top. Figure 5 shows the variability in the space charge inside each of the 22 cloud layers in more detail,
319 with each cloud layer plotted as an individual boxplot. The magnitude of space charge encountered
320 during these flights is in agreement with previously reported values of stratiform cloud charge, which is
321 typically found to be up to 1000 pC m^{-3} (e.g. Imyanitov and Chubarina, 1967; Nicoll and Harrison, 2009;
322 Nicoll and Harrison, 2010; Nicoll 2013)
323
324 Figure 2 presents measurements from an individual cloud/charge sensor flight through a stratiform cloud,
325 which demonstrates agreement with theoretical expectations in terms of the location and polarity of the
326 cloud edge charge layers, however the boxplots in Figure 5 show that considerable variability in charge
327 can exist between different cloud layers. Figure 6 further demonstrates the variability between different
328 cloud layers by showing the individual vertical profiles from 16 of the 22 stratiform clouds sampled,
329 normalised by the measured cloud depth. Only clouds with mean altitude <3km were selected as these
330 lie within the typical altitude for stratocumulus clouds, and below this altitude the ion production rate
331 varies less with height than at higher altitudes (see section 5.2). Figure 6(a) shows the in-cloud visibility
332 as calculated from measurements from the cloud droplet sensor using the method explained in section
333 3.1, and (b) the space charge density measured by the charge sensor. There is obvious variability in both
334 the shape of the vertical profiles and magnitude of the space charge between individual cloud layers. It
335 is therefore useful to consider the average profile through a stratiform cloud layer (Figure 6 (c) and (d)).
336 Figure 6(d) demonstrates that, as in the case of the individual cloud layer shown in Figure 2, on average,
337 positive charge exists at the cloud top region, and negative charge in the cloud base. At the cloud top, the

maximum mean charge is +32 pC m^{-3}, and at the base -24 pC m^{-3}, suggesting an asymmetry between cloud top and cloud base. The theoretical expectation is that this results from the vertical conductivity gradient, which, in general is larger at cloud top than in the base (see Harrison et al 2015), and discussed in more detail here in section 5.1. It is also interesting to note that, on average, the negatively charged region is relatively shallow and rapidly reaches a maximum value (at~ 20% cloud depth fraction), whilst the positively charged region is more vertically extensive (from 40-90% of the cloud depth fraction). The fact that charge is observed away from the upper and lower cloud boundaries is likely to be due to mixing of charge through vertical motion from updrafts and downdrafts within the cloud volume. Although the stratiform nature of the clouds will minimise vertical motions, local variability and updrafts of up to 1ms^{-1} nevertheless occur (e.g. Peng et al, 2005). An asymmetry in the vertical extent of updrafts compared with downdrafts will result in different mixing profiles between cloud top and cloud base, which would influence the vertical extents of average positive and negative charge regions. Although the polarity of the average vertical space charge profile agrees with theoretical predictions, on an individual cloud to cloud basis, considerable variability exists. This was originally documented by Imyanitov and Chubarina (1957) in a series of aircraft flights measuring electric field, E_z, from which the space charge profiles could be derived using equation 1. They found that only 41 % of 70 flights contained positive charge in the upper regions and negative charge in the base, with a mean space charge density of 7.3 pC m^{-3} in the upper part, and -5.3 pC m^{-3} in the lower part. Similarly to Imyanitov and Chubarina (1957), the instrumented balloon flights from Reading, Hyytiala and Halley find that 57% of the 22 sampled stratiform clouds contain positive charge in their upper regions, and negative charge in the lower regions, whilst only 5% (1 flight) have an inverted charge polarity structure (i.e. negative charge at top and positive in base). 33% of cloud layers contained positive charge at both cloud top and base, and 5% (i.e. 1 flight) negative charge at cloud top and base. Thus, on average the charge structure within low level stratiform clouds agrees with that predicted by theory, but individual clouds may not. This is likely to be attributable to the oversimplification of cloud edge charging theory, which does not take into account the dynamical motions within a cloud. For example, the existence of entirely positively charged clouds may be due vertical mixing processes which act to transport positive charge

365 downwards into the base of the cloud. The observed asymmetry between cloud top and cloud base
366 charge could hypothetically cause positive charge to dominate over the negative, thus leading to a net
367 positive charge throughout the cloud. The extent to which the theory holds for the set of measured layer
368 clouds will be examined in the next section.
369 -
370 **5. Factors controlling cloud edge charging**
371 Equation 3 describes the cloud edge charge in solely steady state electrostatic terms, specifically the
372 variation with height of the air conductivity and the local vertical conductivity gradient. This section will
373 now deal with each of these factors in turn.
374
375 **5.1 Conductivity gradient**
376 One property which shows great variability between clouds is the thickness of the transition zone
377 between clear air and the horizontal cloud edge, which is directly related to the vertical gradient in
378 conductivity, and also the generation of space charge in accordance with equation 3. A direct
379 measurement of the cloud edge transition zone thickness can be obtained from the optical measurements
380 made by the cloud droplet sensor. An example of a particularly narrow (or "sharp") cloud edge transition
381 zone is shown in the cloud layer in figure 3, where the optical transition from cloud to clear air at the
382 cloud top takes place over a depth of 30m. In this cloud layer the space charge within the cloud top is co-
383 located exactly where the optical cloud changes occur, with the magnitude of the space charge increasing
384 as the visibility decreases. The charge at cloud top in this particular cloud layer is so large that it saturated
385 the charge sensor (giving a lower limit of charge as >200pCm^{-3}). The same cannot be said for the cloud
386 base region, however, which has a much less distinct change from clear to cloudy air, and hence no
387 appreciable amount of space charge is located in the cloud base region. For all of the 22 stratiform
388 clouds studied here the nature of the cloud top and cloud base transitions, with the cloud top transition
389 extending vertically over a narrower region, is consistent between clouds. This is expected from the often
390 sharp temperature inversion in the cloud top region, which acts as a lid to further upward motion, which

391 is not present in the cloud base region. The magnitude of the charge which accumulates at horizontal
392 cloud edges is therefore constrained by thermodynamical processes.
393
394 Figure 7 shows boxplots of the cloud edge transition zone thickness, visibility gradient and space charge
395 measured at both horizontal cloud edges of cloud top and cloud base for 16 of the cloud layers with
396 altitudes <3km. The cloud base was identified on the basis of determining where the optical cloud droplet
397 sensor voltage began increasing, and cloud top from where it was decreasing. The cloud edge transition
398 zone thickness was also selected on this basis. It is seen that in general, the cloud edge transition zone is
399 narrower at cloud top (median depth 72m) than cloud base (median depth 128m). Similarly the gradient
400 in visibility (which is related to the cloud droplet concentration and conductivity by equations 5, 6 and 7),
401 is also larger at cloud top (42) than cloud base (21). In agreement with this, the magnitude of the space
402 charge in cloud top regions is also greater at cloud top (median 45 pCm^{-3}) than at cloud base (median 29
403 pCm^{-3}), demonstrating an asymmetry in charge between cloud top and cloud base. It follows that the
404 largest magnitude of cloud edge charging will occur in stable stratified layers with sharp edges and little
405 vertical mixing. These properties are typical of marine stratocumulus, which are characterised by strong
406 temperature inversions at cloud top.
407
408 **5.2 Conductivity and altitude variation**
409 Conductivity varies substantially with height because of the variation in cosmic ray ion production, and
410 contribution from radon near the surface, therefore to investigate the height dependence of cloud edge
411 charge it is first necessary to determine the vertical profile of conductivity. Conductivity profiles can be
412 measured directly e.g. by a Gerdien type sensor (e.g. Nicoll and Harrison, 2008) or indirectly by measuring
413 the ion production rate. Measurements showing the ion production rate variation with height have been
414 presented by Harrison et al, 2014 using the balloon-borne Geiger sensor described in section 3.1. In this
415 study measurements of vertical profiles of ionisation rate have been obtained at all three cloud
416 measurement sites of Reading, Hyytiala and Halley which allow the average vertical ion production rate

417 profile from the surface up to 5km for all of the sites together to be found, as well as the clear air
418 conductivity profile (shown in Figure 8 (a)).

419

420 To determine the effect of cloud height on the generated space charge an estimate of the in-cloud
421 conductivity profile has been derived from the cloud droplet profile of the cloud shown in Figure 2, typical
422 of the average cloud profile, and equation 6. The predicted magnitude of the mean space charge in the
423 cloud is then calculated from equation 3, using the calculated conductivity values from Figure 8 (a). This
424 is then compared with the measured mean value (magnitude) of space charge measured from all 22 cloud
425 layers at the 3 measurement sites (where the predicted and measured values of charge are shown as the
426 grey line and black points in Figure 8 (b) respectively). It is seen that the predicted space charge follows
427 closely the inverse variation in ionisation rate with height, with a reduction in ionisation at approximately
428 1km where the radon contribution falls off. Although the same variation is not so evident in the measured
429 space charge values, the black line depicts a lowess fit to the data (locally weighted scatterplot regression)
430 which does demonstrate elevated space charge values in the lowest 1.5km, which falls off rapidly with
431 increasing height. This is supported by the boxplot in Figure 8 (c) which divides the measured mean space
432 charge values according to the height of cloud in which they were measured. It is clear that there is a
433 statistically significant difference (at the 95% confidence level) in the mean space charge measured in
434 clouds below 2km and above 2km, with lower altitude clouds being more highly charged. The median of
435 the mean space charge distribution for the low altitude (<2km) clouds is 20.2 pCm^{-3}, and 7.0 pCm^{-3} for the
436 higher altitude clouds (>2km). The ratio of these two space charge values is 2.9 which is very similar to
437 the ratio of mean conductivity (=2.8) below and above 2km from Figure 8(a). There is also a noticeable
438 difference in the range of the space charge values between the two altitude ranges, with the inter-quartile
439 range (IQR) = 11.5 pC m^{-3} for low altitude clouds compared to IQR = 5.4 pC m^{-3} for the higher altitude
440 clouds, potentially related to the smaller magnitude of space charge in the higher altitude clouds. The
441 data shown in Figure 8 thus supports the hypothesis that the droplet charging effect is greatest for low

442 altitude stratiform cloud, which would be particularly so over the oceans, where any radon contribution
443 to the total ionisation rate is negligible.
444
445 Substantial scatter in the data points is expected as a number of factors influence the space charge
446 generation in clouds in addition to the conductivity profile. No allowance has been made here for
447 differences in cloud edge transition zone thickness between low altitude and high altitude clouds, which
448 may result from dynamical changes between the different cloud altitudes. Further, it should be noted
449 that the assumption of using the average cloud droplet profile for all altitudes of cloud between 1 and
450 5km is another potential source of variability, which also does not take account of dynamical changes in
451 clouds that typically occur with altitude changes. Although it would be preferable to repeat this analysis
452 to take these points into consideration, as well plot the data from each of the three measurement sites
453 individually, the small number of data points limits the statistical analysis possible.
454
455 **6. Cloud droplet charging**
456 The results shown in section 4 combined with theory provide strong evidence that widespread charging
457 occurs within the edge regions of stratiform cloud layers. Simultaneous charge and cloud droplet
458 measurements also indicate that the charge is likely to reside primarily on the cloud droplets, since charge
459 is typically observed to be present mainly within the region where the visual range indicates that cloud is
460 present. As mentioned in section 1, there are several physical consequences associated with the charging
461 of cloud droplets, including modification of droplet-particle interactions and droplet activation, however
462 the extent to which the droplet behaviour is influenced depends on the magnitude of the droplet charge.
463 Since most of the space charge within a cloud will reside on cloud droplets it is possible to represent the
464 measured space charge density values discussed in section 4 in terms of elementary charges per droplet,
465 rather than charge per unit volume. If the charge density ρ is assumed to be partitioned equally between
466 cloud droplets with concentration, Z_d, the mean number of elementary charges per droplet *j* is given by

467 $$j = \frac{\rho}{Z_d e} \quad (7)$$

468 Summary histograms of individual cloud droplet charges are shown in Figure 9 for (a) cloud base and (b)
469 cloud top regions, for all 16 cloud layers with altitude <3km (with cloud base and top selected on the basis
470 of changes in the optical cloud droplet sensor response, as for Figure 7). For each cloud layer, equation
471 7 was applied to the measured space charge values, together with the calculated equivalent cloud droplet
472 number concentration profile (calculated assuming cloud droplets are monodisperse with 10μm
473 diameter). At cloud base, the range of cloud droplet charges from Figure 9 (a) is -270 to 57e, with median
474 -0.4e, whilst at cloud top droplet charges range from -26 to 31e, with median 1.4e. Since the droplet
475 charge is calculated directly from the space charge measurements, overall the droplet charges are largely
476 negative at cloud base and positive at cloud top, with a slight asymmetry between the two in that cloud
477 droplet charges at the cloud top are slightly larger than in the base.

478

479 **7. Discussion**

480 This work presents the first quantitative comparison of multiple observations of stratiform cloud edge
481 charging from multiple sites. Although general agreement between observations and theory in the
482 location and polarity of the charge layers is found on average across all the soundings, substantial local
483 differences are apparent in individual clouds. The results discussed here therefore demonstrate that cloud
484 edge charging is dependent on both the dynamical properties of the cloud as well as the background
485 electrical environment. Turbulence and updrafts and downdrafts inside the cloud layer will act to mix the
486 charge generated at the cloud edges, and the presence of ice as well as varying aerosol concentrations
487 (which are not considered here) are also likely to play a role in the resultant charge profile.

488 The confirmation of the asymmetry in charging between cloud base and top is an important factor which
489 has hitherto not been included in modelling studies of layer cloud electrification, and has potentially
490 important consequences for larger charging of droplets at cloud top than base. In terms of the
491 implications for cloud microphysical processes, the magnitude of the estimated droplet charges (from a

few *e* per droplet to 270*e*) are large enough to affect droplet-droplet collision processes, but likely not droplet activation, which is thought to require charges of ~1000*e*. Harrison et al (2015) describes the increased collision rate between small and large droplets when both droplets are equally charged through an increase in the collision efficiency (i.e. the likelihood of droplets colliding with each other), which results from the mutual attraction of the droplets from the electrical image force. This occurs even when the droplets have the same polarity of charge (as would typically be the case in an unmixed cloud layer), and will be most dominant for droplets (<2μm), likely resulting in a depletion in the number concentration of small droplets.

Over-range of the charge sensor occurred on one flight (shown in Figure3), demonstrating that space charge regions >200pCm^{-3} can exist within stratiform clouds. Measurements from the optical cloud droplet sensor presented here provide a more realistic value of cloud edge depth of ~100m than that previously used in modelling studies (e.g. 11m in Zhou and Tinsley, 2007), and the large variability observed in the charge profiles on an individual cloud to cloud basis suggest that the simple modelling approach adopted up to now needs to be extended for future studies. These therefore present a unique dataset of in-cloud stratiform charge measurements which can help to inform future modelling studies of cloud droplet charging effects on cloud microphysics (e.g. Harrison et al 2015; Zhou and Tinsley 2012; Tinsley and Leddon 2013).

Although not considered in detail here, variations in the air Earth conduction current may also contribute to some of the variability in cloud edge charging since it is the flow of this vertical current through cloud layers which leads to the accumulation of space charge at cloud edges. J_c is controlled by a number of factors internal to Earth's climate system, which are mainly associated with the Global atmospheric Electric Circuit (GEC). This is driven by global thunderstorm activity, therefore changes in thunderstorm output current and lightning activity (which are known to be linked to surface temperature changes and global weather patterns such as ENSO (Harrison et al. 2011; Williams 1992) will act to increase or decrease J_c. Variations in the vertical conductivity profile, such as from volcanic eruptions, or even the presence of

518 cloud layers themselves (e.g. Baumgaertner et al 2014, Zhou and Tinsley 2010, Nicoll and Harrison 2009)
519 also play a role in modulating J_c. Conductivity variations also occur, more dominantly, through external
520 factors such as changes in the GCR flux (e.g. decreases in global ionisation rates of up to 10% can occur
521 during Forbush decreases, typically associated with explosive events on the sun), and also from solar
522 proton events. Understanding the effects of space weather on the GEC and therefore J_c should therefore
523 remain an area of active research, particularly as solar disturbances have the potential to affect cloud
524 edge charging through the mechanism discussed here (see Nicoll 2014 and Mironova et al 2015 for recent
525 reviews). There is no doubt that assessing the importance of the role that J_c plays in modulating cloud
526 edge charging is difficult to do. Measurements of J_c are sparse, and because significant variability in cloud
527 charge profiles exists between individual cloud layers, a larger statistical sample of cloud charge data is
528 therefore required to properly assess this important factor.
529

530 **8. Conclusions**

531 These results represent the first multiple site comparison of non-thunderstorm cloud charge, and the first
532 study to undertake simultaneous high vertical resolution measurements of cloud droplet and charge
533 properties in multiple cloud layers and compare them with theoretical charging expectations. The cloud
534 and charge data demonstrates unequivocally that all stratiform clouds can be expected to contain charge
535 at their upper and lower boundaries to varying extent, due to vertical current flow in the Global
536 atmospheric Electric Circuit. On average, charge is found near upper and lower cloud edges and the cloud
537 edge charge polarity (positive at cloud top and negative at cloud base) agrees with theory, but large
538 variations in both location and polarity of charge are observed within individual cloud layers, likely due to
539 dynamical processes within the clouds, which are at present not included in theoretical models of cloud
540 edge charging.
541

542 The results also demonstrate that a combination of cloud thermodynamics with the background electrical
543 conditions contribute to the magnitude of cloud edge charging in terms of the “sharpness” of the cloud

544 edge transition zone thickness. This is observed in terms of an asymmetry between cloud top and base
545 charge, typically with larger charge observed at cloud top (32 pCm^{-3} compared to 24 pCm^{-3} in the cloud
546 base) due to the more rapid transition from cloudy to clear air which often occurs due to a significant
547 temperature inversion in the cloud top region.
548
549 Finally, the difference in cloud charge robustly observed between low altitude (<2km) and higher altitude
550 stratiform clouds (2-5km) demonstrates the important role of cosmic ray ionisation in the cloud edge
551 charging process, if the other edge properties of clouds remain unchanged. This confirms the theoretical
552 expectation that layer cloud electrification will be at its greatest for low level clouds.
553
554 **Acknowledgements**
555 NERC grant NE/H002081/1 and STFC grant ST/K001965/1 supported the radiosonde sensor development.
556 KAN also acknowledges an Early Career Fellowship of the Leverhulme Trust (ECF-2011-225), a NERC
557 Independent Research Fellowship (NE/L011514/1), NERC Collaborative Gearing Scheme (CGS) grant and
558 ACTRIS TransNational Access funding from the European Union Seventh Framework Programme
559 (FP7/2007-2013) under grant agreement n° 262254. Logistics support for Hyytiala launches was
560 supported by the Office of Biological and Environmental Research of the U.S. Department of Energy as
561 part of the Atmospheric Radiation Measurement (ARM) Climate Research Facility, an Office of Science
562 user facility. Technicians in the Department of Meteorology at the University of Reading assisted with
563 sensor assembly and the majority of the balloon launches. Assistance with additional balloon launches
564 was provided by ARM AMF2 technicians at Hyytiala, and staff at the British Antarctic Survey research
565 station at Halley. The satellite image in figure 7 is courtesy of NERC Satellite Receiving Station, Dundee
566 University, Scotland: http://www.sat.dundee.ac.uk/. The balloon flight data used in the analysis is
567 archived through the University of Reading Data repository at http://researchdata.reading.ac.uk/38/.
568

569 **Appendix. Effective area of charge sensor**

570 The balloon-borne charge sensor used to provide the in-cloud charge measurements employs an
571 approximately spherical electrode connected to a sensitive electrometer, and primarily responds to
572 induced displacement currents generated by electric field changes as the sensor moves through the cloud
573 layer. A full description of the sensor electronics is given by Nicoll, 2013, with further details of the
574 calculation of cloud space charge given here.

575

576 The electrometer circuit comprises a current to voltage converter employing a T-network of resistors to
577 synthesise a total effective resistance, R = 2.4 x 10^{11} Ω. The induced current, *i*, is related to the final output
578 voltage of the electrometer circuit, V_{out}, by

579 $$i = \frac{Vout}{R} \quad \text{A1.}$$

580 To calculate the space charge density, *ρ*, first consider the charge, *Q*, induced on a stationary sensor
581 electrode due to the electric field. This is given by Gauss' law as

582 $$Q = -A_{eff}\varepsilon_0 E \quad \text{A2,}$$

583 where A_{eff} is the effective area of the electrode i.e. the area of the conductor on which the field lines end,
584 which is not necessarily the same as its geometrical surface area. If the sensor is allowed to move, for
585 example by ascending vertically through a cloud layer, the electric field will change, and the induced
586 charge is no longer constant, causing an induced current, *i*, to flow, measured by the electrometer and
587 given by

588 $$i = \frac{dQ}{dt} = -A_{eff}\varepsilon_0 \frac{dE}{dt} = \frac{V_{out}}{R} \quad \text{A3.}$$

589 For vertical motion on a free balloon with ascent rate *w*, the *dE/dt* term in equation A3 is

590 $$\frac{dE}{dt} = \frac{dt}{dz}\frac{dE}{dt} = \frac{1}{w}\frac{dE}{dz} \quad \text{A4,}$$

591 and therefore the current measured by the electrometer is related to the electric field gradient by

592 $$i = -A_{eff}\varepsilon_0 \frac{1}{w}\frac{dE}{dz} \quad \text{A5.}$$

593

From equation 1 and equation A5 and substituting for the dE/dz term, it follows that the space charge, ρ, measured by the charge sensor is related to the measured current by

$$\rho = \frac{i}{A_{eff} w} \quad \text{A6.}$$

The unknown quantity in equation A6 is the effective area term, $A_{eff.}$ This can be determined from experimental calibration using equation A3, by placing the charge sensor in a varying electric field which is known.

The experimental calibration was undertaken by measuring the atmospheric electric field in fog (using an electric field mill at the Reading University Atmospheric Observatory (RUAO)) and placing the charge sensor nearby. (The field mill was previously standardised for its form factor using the passive wire antenna method, Bennett and Harrison 2006a.) Fog typically causes the atmospheric electric field to increase and become variable thus generating a sufficiently large dE/dt with which to calibrate the charge sensor. Figure A1 shows a time series of the rate of change of electric field (measured by the field mill, in black) and the current measured by the charge sensor during a 3 hour period of fog. The extremely good correlation between the two traces (Pearson correlation coefficient = 0.75) demonstrates that not only does the balloon charge sensor respond well to changes in electric field, and thus space charge, but its dE/dt response is very similar to that of the commercially available field mill. Figure A2 shows the relationship between the current measured by the charge sensor and dE/dt measured by the field mill.

The effective area of the charge sensor electrode can thus be found from a linear fit between i and dE/dt (Figure A2) as

$$i = -A_{eff} \varepsilon_0 \frac{dE}{dt} \quad \text{A7,}$$

from which it is calculated that A_{eff} = 0.0196 m^2. This can be compared to the approximate surface area of a perfectly spherical electrode (with radius 0.6cm), A = 0.000452 m^2, i.e. approximately 43 times smaller than the effective area, which is reasonable considering the likely electric field distortion from the

relatively complex geometry of the charge sensor electrode. The final space charge value is then computed using A_{eff} above and equation A6, using the local ascent rate in the cloud as found by the radiosonde height information.

References

Allee, P.A., and B.B. Phillips, 1959. Measurement of cloud-droplet charge, electric field, and polar conductivities in supercooled clouds. *J. Atmos. Sci.* **16**, 4, 405-410.

Baumgaertner, A.J.G., G.M. Lucas, J.P. Thayer, and S.A. Mallios, 2014. On the role of clouds in the fair weather part of the global electric circuit. *Atmos Chem and Phys*, 14, 16, 8599-8610 10.5194/acp-14-8599-2014

Bazilevskaya, G. A., et al., 2008. Cosmic ray induced ion production in the atmosphere. *Space Science Reviews,* 137, 149-173.

Beard K.V. and S.N. Grover, 1974. Numerical collision efficiencies for small raindrops colliding with Micron Size Particles. *J Atmos Sci*, **31**, 2, 543-550.

Blakeslee, R.J., D.M. Mach, M.G. Bateman, J.C. Bailey, 2014, Seasonal variations in the lightning diurnal cycle and implications for the global electric circuit, *Atmospheric Research*, **135–136**, 228-243.

Bohren C.F. and D.T. Huffman, 1983. Absorption and scattering of light by small particles. Wiley: new York.

Bricard, J., 1965, Action of radioactivity and of pollution upon parameters of atmospheric electricity, in Problems of Atmospheric and Space Electricity, edited by S. C. Coroniti, pp. 82– 117, Elsevier, Amsterdam.

Gunn, R., 1954. Diffusion charging of atmospheric droplets by ions and the resulting combination coefficients. *J. Meteorol*, **11**, 339–347.

Harrison R.G., 2012. Aerosol-induced correlation between visibility and atmospheric electricity. *J. Aerosol Sci*, **52**, 121–126.

Harrison, R.G., and K.S. Carslaw, 2003. Ion–aerosol–cloud processes in the lower atmosphere. *Rev Geophys*, **41** (3), 1012, 10.1029/2002RG000114.

Harrison, R.G., and M.H.P. Ambaum, 2008. Enhancement of cloud formation by droplet charging. *Proc. R. Soc. A.* **464**, 2561-2573.

Harrison, R.G., K.A. Nicoll and A.G. Lomas, 2012. Programmable data acquisition system for research measurements from meteorological radiosondes *Rev Sci Instrum* **83**, 036106 doi: 10.1063/1.3697717

Harrison, G., Joshi, M. and Pascoe, K., 2011. Inferring convective responses to El Niño with atmospheric electricity measurements at Shetland. Environmental Research Letters, 6, 044028 , doi: 10.1088/1748-9326/6/4/044028

Harrison, R. G. and Ambaum, M. H.P., 2013, Electrical signature in polar night cloud base variations. Environmental Research Letters, 8, 015027, doi: 10.1088/1748-9326/8/1/015027

Harrison, R.G., K.A. Nicoll and A.G. Lomas, 2013, Geiger tube coincidence counter for lower atmosphere radiosonde measurements, Rev. Sci, Instrum., **84**, 076103.

Harrison, R.G., and K.A. Nicoll, 2014. Active optical detection of cloud from a balloon platform *Rev Sci Instrum,* 066104 doi: 10.1063/1.4882318

672 Harrison, R. G., Nicoll, K. A. and Aplin, K. L., 2014. Vertical profile measurements of lower troposphere
673 ionisation. Journal of Atmospheric and Solar-Terrestrial Physics, 119. 203-210, doi:
674 10.1016/j.jastp.2014.08.006

675 Harrison, R.G., Nicoll, K.A. and Ambaum, M. H. P. , 2015. On the microphysical effects of observed cloud
676 edge charging. Quarterly Journal of the Royal Meteorological Society. ISSN 1477-870X doi:
677 10.1002/qj.2554

678 Hirsikko, Anne, et al. 2007. The ^{222}Rn activity concentration, external radiation dose and air ion
679 production rates in a boreal forest in Finland between March 2000 and June 2006. *Boreal environment*
680 *research* 12.3, 265-278.
681
682 HMSO, K.L., 1982. Handbook of Meteorological Instruments, 7 (Measurement of Visibility and Cloud
683 Height). Meteorological Office, Her Majesty's Stationery Office: London, UK.
684
685 Imyanitov, I.M., and E.V. Chubarina, 1967. *Electricity of the free atmosphere.* Jerusalem: Israel Program
686 for Scientific Translations.
687
688 Israel, H. 1971. *Atmospheric Electricity.* Jerusalem: Israel Program for Scientific Translations.
689
690 Jones, O. C. 1957. Problems in atmospheric ionisation. PhD diss., University of Oxford.
691
692 Jones, O.C., Maddever, R.S. and Sanders, J.H., 1959. Radiosonde measurement of vertical electrical field
693 and polar conductivity. *Journal of Scientific Instruments*, *36*(1), 24.

694 Khain, A., V. Arkhipov, M. Pinsky, M. et al., 2004. Rain enhancement and fog elimination by seeding with
695 charged droplets. Part I: Theory and numerical simulations, *J. App Meteorol* **43**, 1513-1529.
696
697 Klein, S.A., and D.L. Hartmann, 1993. The seasonal cycle of low stratiform clouds. *J. Climate,* **6**, 1587-1606.
698
699 Koren, I., Remer, L. A., Kaufman, Y. J., Rudich, Y., & Martins, J. V., 2007. On the twilight zone between
700 clouds and aerosols. *Geophysical research letters*, *34* (8).

701 Mach, D. M., R.J. Blakeslee, and M. G. Bateman, 2011. Global electric circuit implications of combined
702 aircraft storm electric current measurements and satellite-based diurnal lightning statistics. *J. Geophys.*
703 *Res.,* 116 (D5).
704
705 Miles, N.L., J. Verlinde, and E.E. Clothiaux, 2000. Cloud droplet size distributions in low-level stratiform
706 clouds. *J Atmos Sci* 57, 295-311
707
708 Mironova, I.M, K.L. Aplin, F. Arnold, et al., 2015. Energetic particle influences on atmospheric processes,
709 *Space Science Reviews*, DOI 10.1007/s11214-015-0185-4.
710
711 Nicoll, K.A., 2014. Space weather effects on atmospheric electricity, Weather, 69, 238-241,
712 DOI: 10.1002/wea.2323.

713 Nicoll K. A. and R. G. Harrison, 2008, A double-Gerdien instrument for simultaneous bipolar air
714 conductivity measurements on balloon platforms, *Rev. Sci. Instrum*., **79**, 084502-8.

715 Nicoll, K.A., and R.G. Harrison, 2009. Vertical current flow through extensive layer clouds. *J.Atmos. Sol.-*
716 *Terr. Phys.* **71**, 2040-2046.
717
718 Nicoll, K.A., and R.G. Harrison, 2009. A lightweight balloon-carried cloud charge sensor. *Rev. Sci. Instrum.*
719 **80**, 014501.

Nicoll, K.A., and R.G. Harrison, 2010. Experimental determination of layer cloud edge charging from cosmic ray ionisation, *Geophys. Res. Lett.*, **37**, L13802, doi:10.1029/2010GL043605

Nicoll K.A., 2013. A self-calibrating electrometer for atmospheric charge measurements from a balloon platform, *Rev. Sci. Instrum.* **84,** 096107.

Nicoll, K.A., 2014. Space weather effects on atmospheric electricity, Weather, 69 (9), 238-241, DOI: 10.1002/wea.2323.

Peng, Y., U. Lohmann, *and* R. Leaitch, 2005, Importance of vertical velocity variations in the cloud droplet nucleation process of marine stratus clouds, *J. Geophys.* Res., 110, *D21213,* doi:10.1029/2004JD004922.

Phillips, B.B., and G.D. Kinzer, 1958. Measurement of the size and electrification of droplets in cumuliform clouds. *J. Meteor.* **15**, 369-374.

Rycroft M.J., S. Israelsson, C. Price, 2000. The global atmospheric electric circuit, solar activity and climate change. *J Atmos Sol-Terr Phys* **62**, 1563–1576

Rycroft, M.J., K.A. Nicoll, K.L. Aplin, R.G. Harrison, 2012. Global electric circuit coupling between the space environment and the troposphere, *J. Atmos. Sol. Terr. Phys*., **90-91**,198-211. http://dx.doi.org/10.1016/j.jastp.2012.03.015.

Shupe, M.D., Kollias, P., Persson, P.O.G. and McFarquhar, G.M., 2008. Vertical motions in Arctic mixed-phase stratiform clouds. *Journal of the Atmospheric Sciences*, *65*(4), 1304-1322.

Tinsley, B.A., 2000. Influence of solar wind on the global electric circuit, and inferred effects on cloud microphysics, temperature and dynamics in the troposphere. *Space Science Reviews* **94**, 231–258.

Tinsley, B.A., R.P. Rohrbauch, M. Hei, and K.V. Beard, 2000. Effects of image charges on the scavenging of aerosol particles by cloud droplets and on droplet charging and possible ice nucleation processes. *J. Atmos. Sci.* **57**, 2118-21134.

Tinsley, B.A., and D.B. Leddon, 2013, Charge modulation of scavenging in clouds: Extension of Monte Carlo simulations and initial parameterization, *J. Geophys. Res. Atmos.*, **118**, 8612–8624.

Twomey, S., 1956. The electrification of individual cloud droplets. *Tellus,* **4**, 445-451.

Wilson C.T.R., 1929. Some thundercloud problems. *J Frankl Inst,* **208**, 1–12

Zhou, L., and B.A. Tinsley, 2007. Production of space charge at the boundaries of layer clouds, *J Geophys Res*, **112**, D11203, doi:10.1029/2006JD007998.

Zhou, L. and B. A. Tinsley, 2010, Global circuit model with clouds, J.Atmos. Sci., 67, 1143–1156, doi:10.1175/2009JAS3208.1

Zhou, L. and B.A. Tinsley,2012, Time dependent charging of layer clouds in the global electric circuit, Adv. Space Res., 50,6,828-842.

770 **Figures and Tables**
771

Cloud number	Date	Location	Mean cloud height (m)	Cloud depth (m)	Mean space charge (pCm^{-3})	Max. space charge (pCm^{-3})
1	22/04/13	Reading	1534	446	39±7	204
2	03/07/13	Reading	1846	227	23±6	143
3	04/07/13	Reading	735	640	43±6	253
4	31/07/13	Reading	790	622	30±5	200
5	16/08/13	Reading	720	242	29±6	153
6	16/08/13_2	Reading	1200	90	18±6	151
7	23/08/13	Reading	4553	306	5±1	32
8	31/10/13	Reading	2522	333	9±3	148
9	18/11/13	Reading	1146	328	16±4	174
10	18/11/13_2	Reading	4197	135	2±1	10
11	02/12/13	Reading	1039	174	19±4	97
12	03/12/13	Reading	801	374	21±4	172
13	27/05/14	Hyytiala	4838	163	9±2	75
14	27/05/14_2	Hyytiala	1849	208	16±5	104
15	29/05/14	Hyytiala	3311	120	29±6	113
16	29/05/14_2	Hyytiala	3907	289	11±3	133
17	30/05/14	Hyytiala	2345	86	4±13	52
18	30/05/14_2	Hyytiala	499	178	23±8	127
19	20/02/15	Halley	1011	570	6±1	42
20	21/02/15	Halley	974	577	13±1	92
21	06/03/15	Halley	475	281	5±1	32
22	06/03/15	Halley	3067	1700	4±1	102
Median			**1367**	**285**	**16**	**120**

772
773 Table 1. Details of cloud and charge sensor balloon flights through stratiform clouds from 2013-2015. The
774 mean cloud height is the height of the centre of the cloud and the cloud depth is the difference in height
775 between cloud base and top. The mean and maximum values of space charge are calculated from the

magnitude of the in-cloud space charge for each cloud layer. The uncertainty in the mean charge is 2 standard errors on the mean values which represents the 95% confidence interval. Balloons which encountered several different layers of stratiform cloud on the same flight are denoted by "_2" in the flight date. N.B. all data is from the ascent stage of the flight.

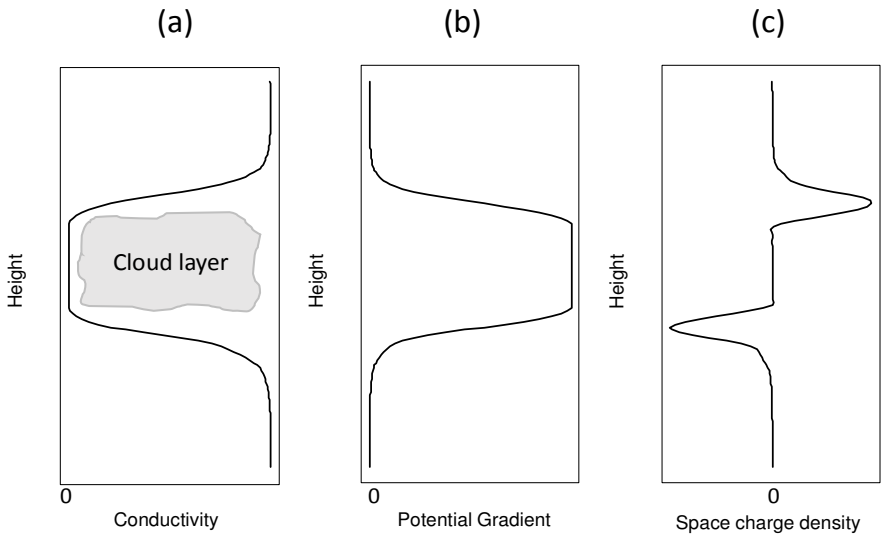

784

785 Figure 1. Hypothetical vertical profiles of atmospheric electrical quantities through a horizontally-

786 extensive stratiform cloud layer (a) conductivity, (b) potential gradient and (c) derived space charge

787 density.

788

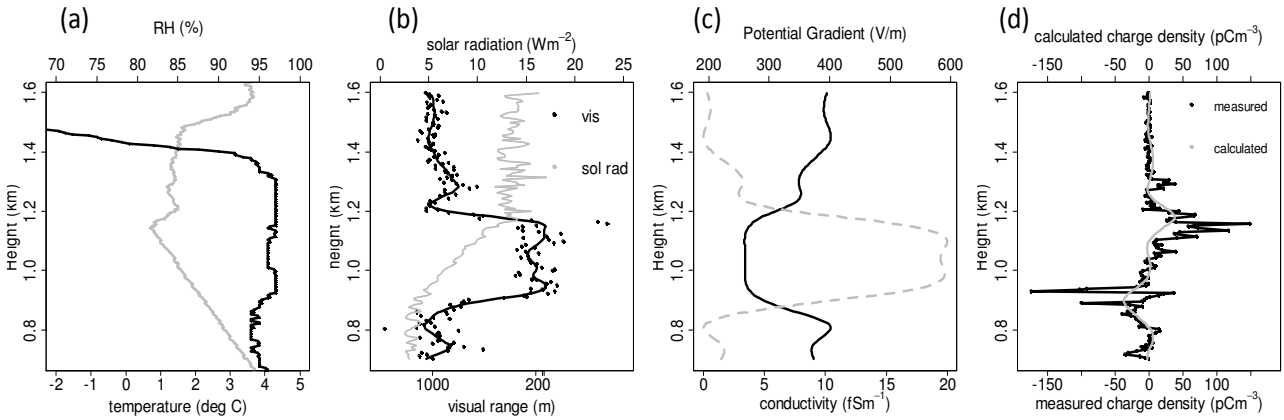

Figure 2. Vertical profile through a stratocumulus layer over Reading University Atmospheric Observatory (RUAO) from a specially instrumented radiosonde. (a) Temperature (grey) and relative humidity (RH) (black) measured by the radiosonde, (b) visual range and downwards solar radiation measured by an optical cloud droplet sensor, (c) derived parameters of electrical conductivity (black) and potential gradient (grey dotted line) using equations 2, and 4-6 and assumptions outlined in section 3.1 , (d) space charge density measured by a charge sensor (black line and data points) plotted alongside the expected space charge (grey line) calculated from the cloud droplet sensor measurements using the theory in section 3.1.

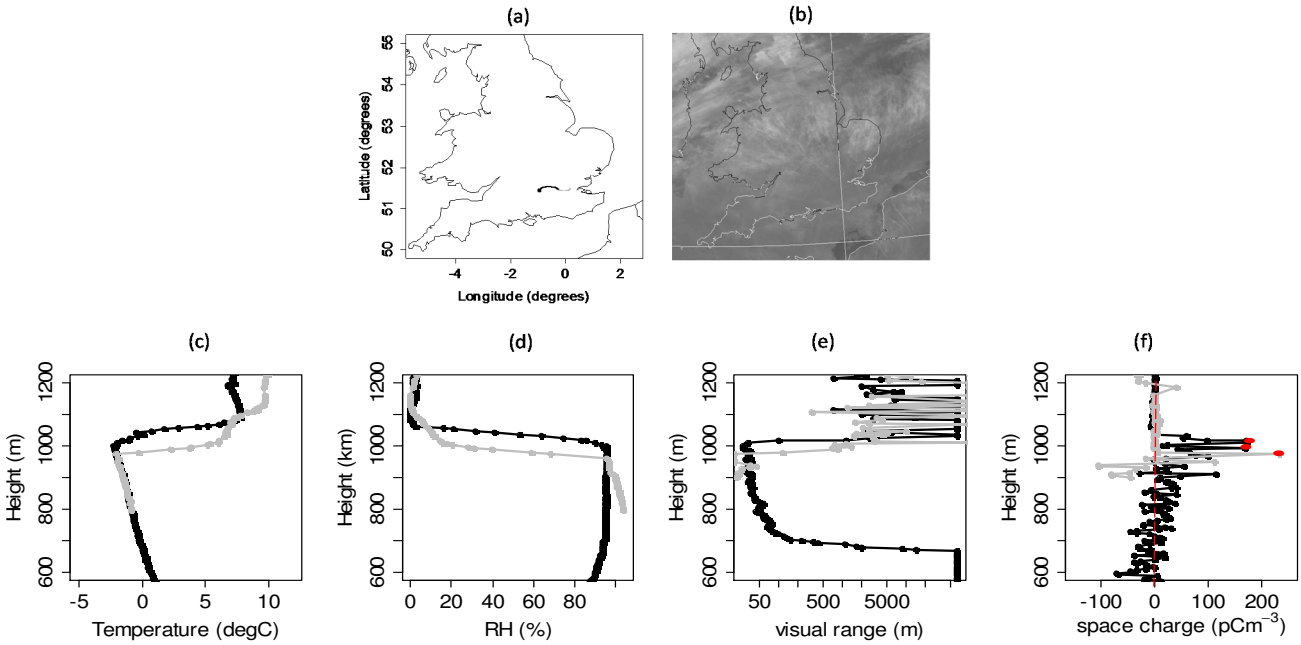

800

801 Figure 3. Ascent and descent of an instrumented balloon flight through the same cloud layer on 03/12/13.
802 (a) shows the flight path of the balloon (ascent in black, descent in grey), launched from Reading, UK. (b)
803 demonstrates the presence of a low level cloud layer widespread over most of the UK as measured by the
804 AVHRR satellite (IR channel 4) at 10:27am, the same time as balloon launch time. Temperature and RH
805 measured by the radiosonde are shown in figures (c) and (d), and data from the cloud and charge sensors
806 shown in figures (e) and (f). Note that the visual range data is plotted on a log scale. Black shows the
807 ascent, grey the descent through the same cloud layer 105 km from the launch point. Red points in (f)
808 denote charge values where the charge sensor saturated therefore these values are a lower estimate of
809 the charge in this region.

810

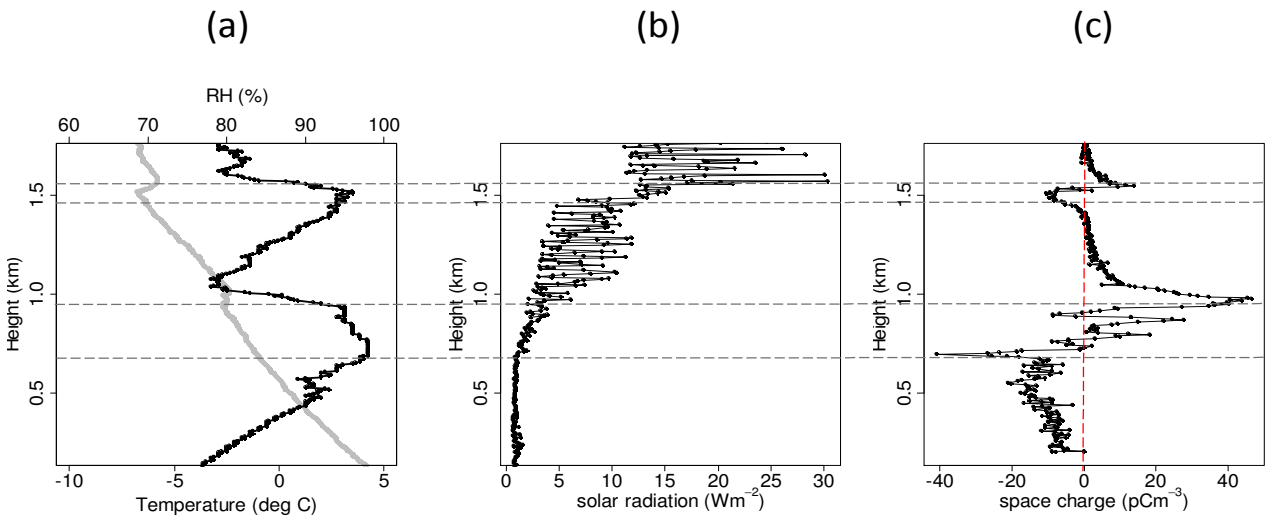

811

812 Figure 4. Vertical profile from an instrumented balloon flight through multiple stratiform cloud layers,
813 launched from Reading on 08/02/13. (a) temperature and RH measured by the radiosonde, (b) solar
814 radiation measured by the passive cloud sensor, (c) space charge measured by the charge sensor. Grey
815 dashed lines denote approximate heights of cloud base and top.

816

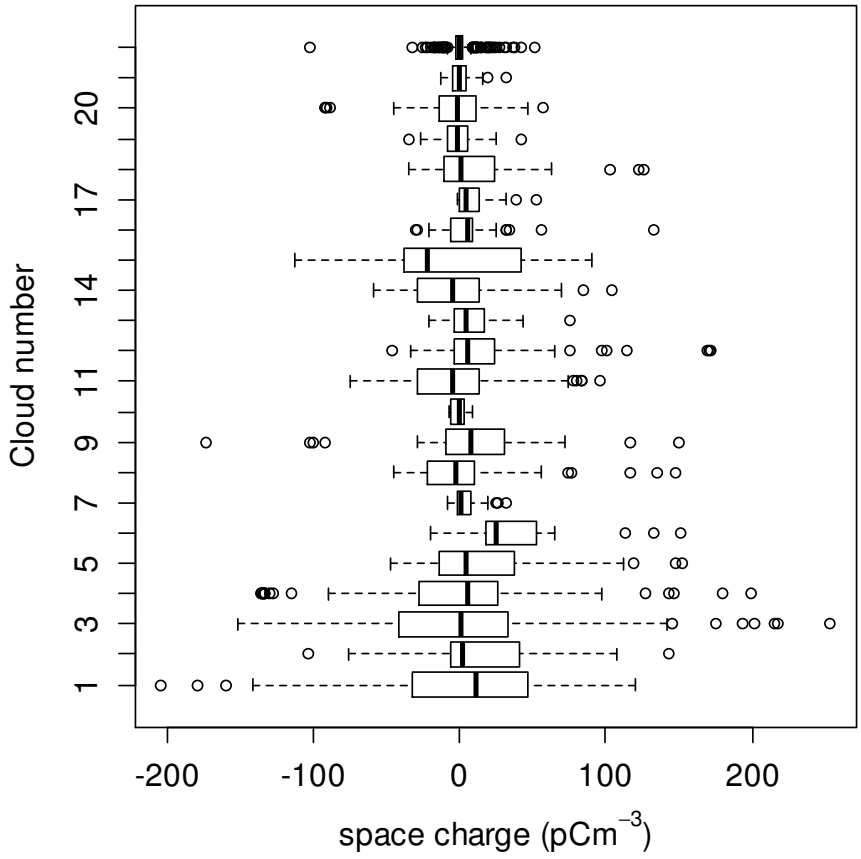

817

818 Figure 5. Boxplot of the space charge distributions within each of the 22 studied cloud layers described in

819 Table 1. The black solid line denotes the median of the distribution and the whiskers the interquartile

820 range.

821

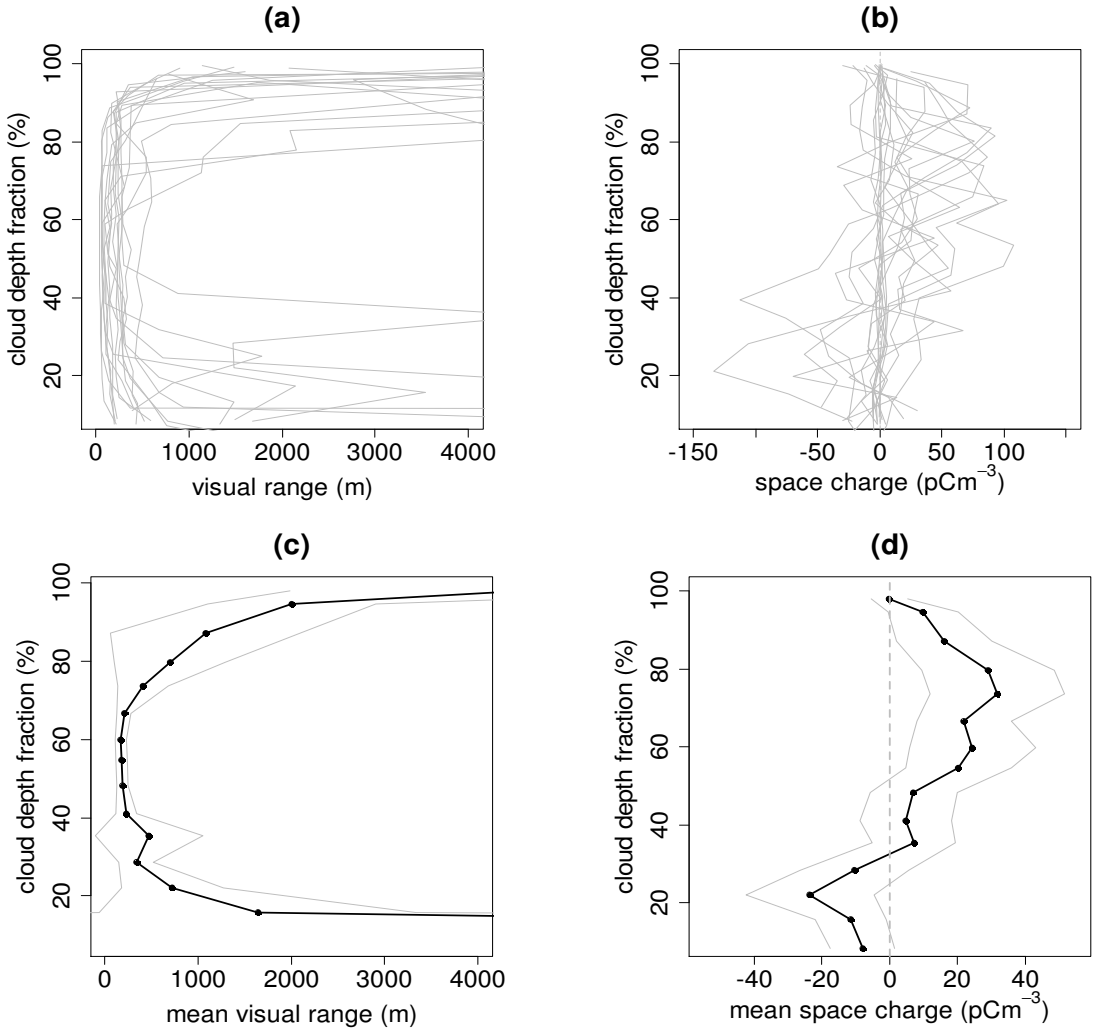

822

823 Figure 6. Profiles from 16 cloud and charge sensor balloon flights through stratocumulus clouds with
824 height <3km. (a) and (b) individual profiles from flights, (c) and (d) average profiles calculated from the
825 16 flights. (a) and (c) visibility derived from cloud sensor, (b) and (d) space charge measured by the charge
826 sensor. The y-axis denotes height normalised by cloud depth, found by dividing each cloud layer into 15
827 evenly spaced altitude layers, where 0% denotes cloud base and 100% cloud top. The data points in (c)
828 and (d) are calculated from the mean of the variables in each of the 15 altitude layers. Grey solid lines in
829 (c) and (d) show two standard errors on the mean values.

830

831

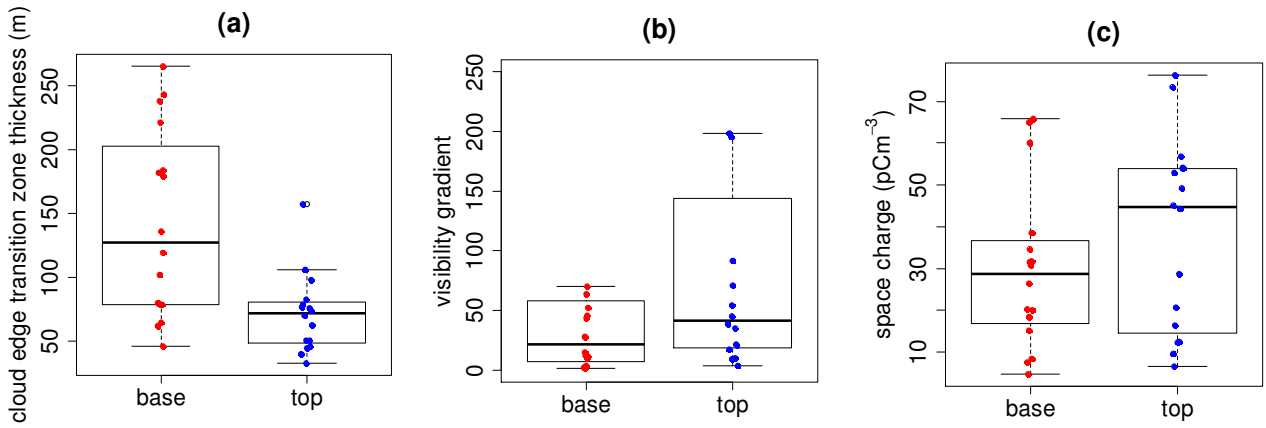

832

833 Figure 7. (a) vertical extent of transition region between cloudy and clear air, (b) gradient in visibility at
834 cloud edge measured by cloud sensor, (c) magnitude of space charge measured by charge sensor. Left
835 hand box plots (left) represent cloud base (red) and right hand plots cloud top (blue). Data are
836 averages over cloud top/base region, where each point represents one cloud edge and only include
837 cloud layers <3km altitude. Cloud base regions are selected on the basis of when the optical cloud
838 droplet sensor voltage was increasing, and cloud top when it was decreasing.

839

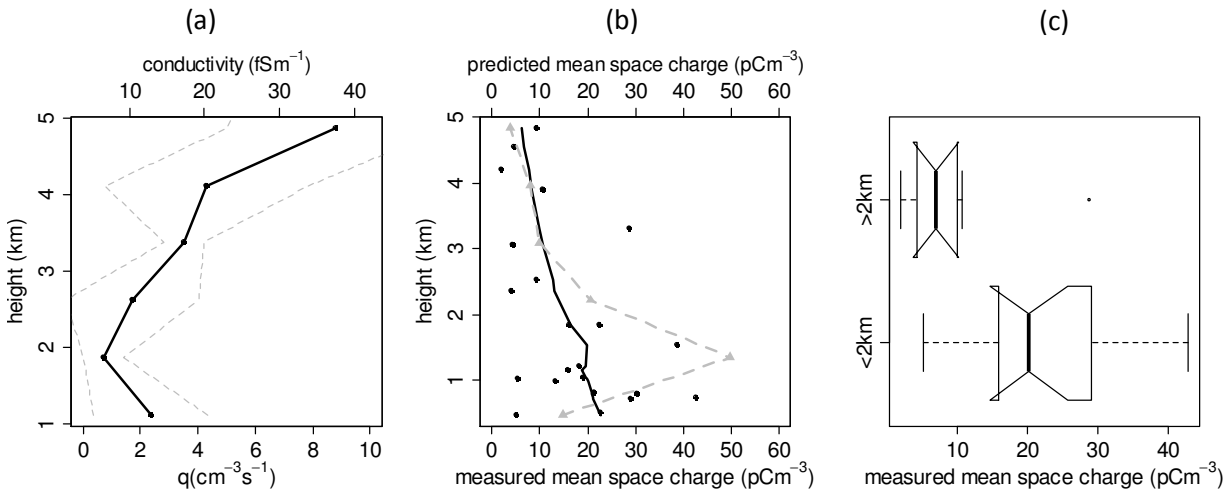

840

841 Figure 8. (a) average vertical profile of ionisation rate measured by a balloon borne Geiger sensor and
842 corresponding conductivity profile calculated from equation 6 for Reading, Hyytiala and Halley between
843 2013 and 2015. Grey lines denote 2 standard errors on the mean values. (b) magnitude of the mean in-
844 cloud space charge (grey dotted line), predicted as a function of height, using the average cloud droplet
845 profile of the case in Figure 2, and the ambient conductivity profile in Figure 8 (a), and measured mean
846 space charge (absolute values) from all 22 cloud layers at Reading, Hyytiala and Halley (black points and
847 black line, which shows a lowess fit to the data points). (c) boxplot of measured mean space charge values
848 separated into two cloud height ranges, with mean cloud height <2km (14 cloud layers) and >2km (8 cloud
849 layers). The edges and line in the centre of the boxes show the upper and lower quartiles and the median.
850 Notches indicate the 95% confidence limits on the median and whiskers extend to 1.5 times the inter-
851 quartile range.

852

853

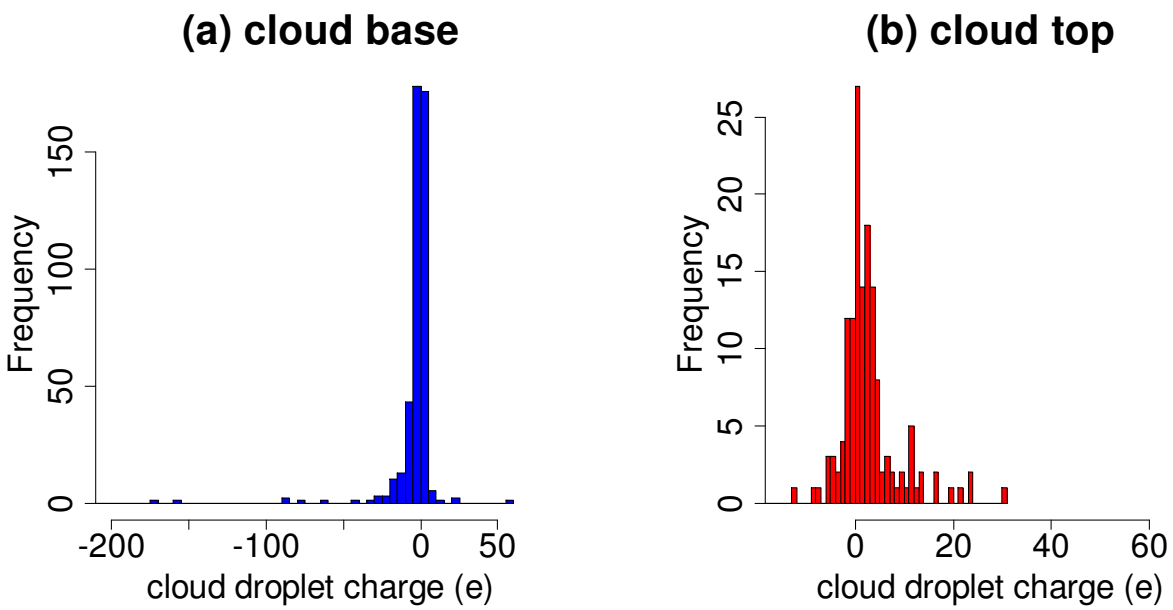

854

855 Figure 9. Histograms of individual cloud droplet charges (in units of elementary charge, e), calculated from
856 measured space charge and calculated equivalent cloud droplet number concentration (assuming cloud
857 droplets are monodisperse with 10μm diameter), for (a) cloud base and (b) cloud top for 16 stratiform
858 cloud layers <3km altitude. (a) contains 444 data points and (b) 147 points, since the cloud top region is
859 typically much shallower than the base.

860

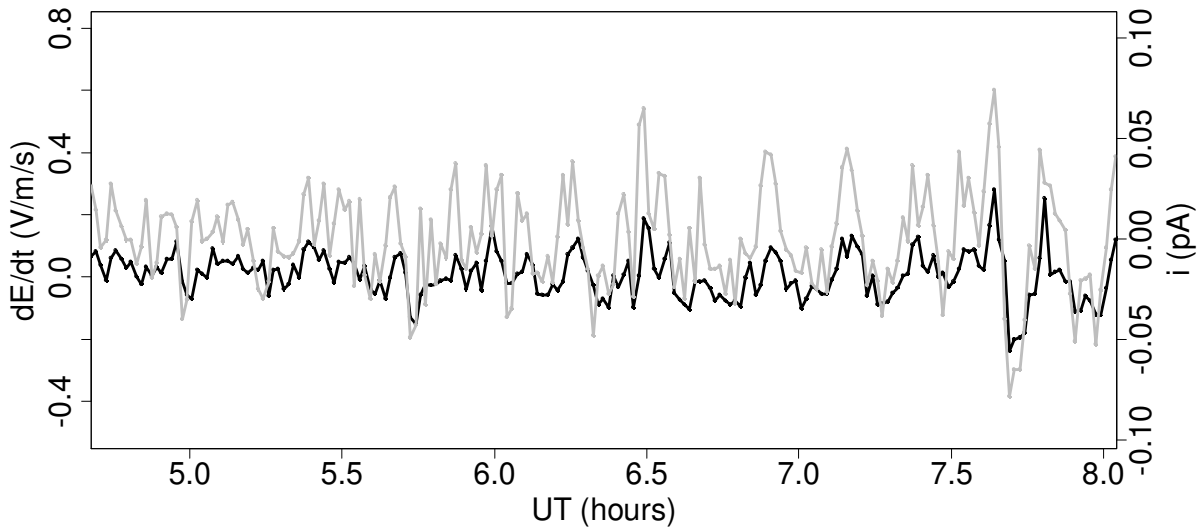

Figure A1. Time series of data from calibration of balloon borne charge sensor in fog on Reading University Atmospheric Observatory (RUAO). The electric field change (dE/dt) measured by a commercial field mill (JCI 131) is shown in black and the corresponding current measured by the charge sensor as a result of the electric field changes shown in grey.

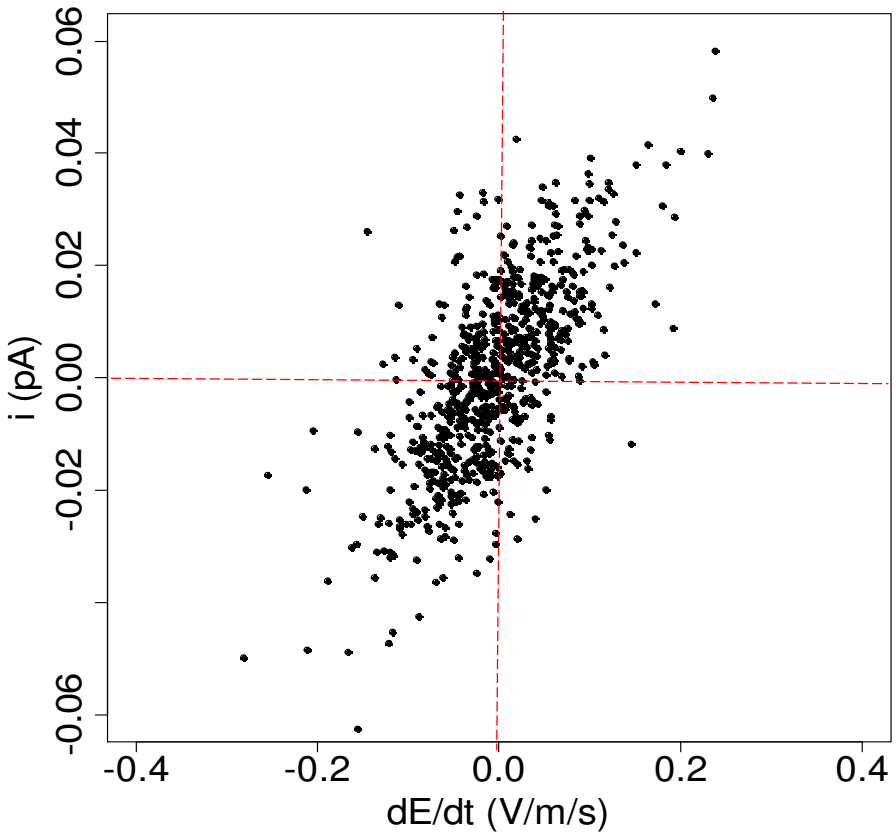

868

869 Figure A2. Calibration of balloon borne charge sensor during fog-induced electric field changes. Sensor
870 electrode current, i, is plotted against simultaneously measured rate of change of electric field (dE/dt)
871 measured by a commercial field mill.

872